An Exponential Constitutive Model Excluding Fibers Under Compression: Application to Extension–Inflation of a Residually Stressed Carotid Artery

Kewei Li[1], Ray W. Ogden[2] and Gerhard A. Holzapfel[1,3†]

[1]Institute of Biomechanics, Graz University of Technology
Stremayrgasse 16-II, 8010 Graz, Austria

[2]School of Mathematics and Statistics, University of Glasgow
University Gardens, Glasgow G12 8QW, Scotland, UK

[3]Faculty of Engineering Science and Technology,
Norwegian University of Science and Technology (NTNU), 7491 Trondheim, Norway

To appear in **Math. Mech. Solids**
May 11, 2017

Abstract. Detailed information on the three-dimensional dispersion of collagen fibers within layers of healthy and diseased soft biological tissues has been reported recently. Previously we have proposed a constitutive model for soft fibrous solids based on the angular integration approach which allows the exclusion of any compressed collagen fiber within the dispersion. In addition, a computational implementation of that model in a general purpose finite element program has been investigated and verified with the standard fiber-reinforcing model for fiber contributions. In this study, we develop the proposed fiber dispersion model further using an exponential form of the strain-energy function for the fiber contributions. The finite element implementation of this model with a rotationally symmetrical dispersion of fibers is also presented. This includes explicit expressions for the stress and elasticity tensors. The performance and implementation of the new model are demonstrated by means of a uniaxial extension test, a simple shear test, and an extension–inflation simulation of a residually stressed carotid artery segment. In each example we have obtained good agreement between the finite element solution and the analytical or experimental results.

Keywords: Constitutive modeling; carotid artery; fiber dispersion; residual stress; exclusion of compressed fibers

[†]To whom correspondence should be addressed. Email address: holzapfel@tugraz.at

1 Introduction

Recent studies on the imaging and visualization of the microstructures of soft biological tissues by using, e.g., second-harmonic generation [1], have revealed detailed information about the three-dimensional (3D) organization of collagen fibers in layers of healthy and diseased tissues [1–5]. In many of these tissues the collagen fibers are distributed around a mean direction in the reference configuration in the ground substance within which the fibers are embedded [1, 5–8]. This type of dispersed fiber distribution has been found in human arterial tissues [1, 5], the myocardium [9, 10], corneas [11, 12], articular cartilage [13] and other tissues. Currently, there exist two main approaches for representing fiber dispersion in a constitutive equation: direct incorporation in a strain-energy function through a probability density function (PDF) [14] or by using a generalized structure tensor [15]. These two approaches are referred to as 'angular integration' (AI) and 'generalized structure tensor'(GST) , respectively. A short survey of the main continuum mechanical models which take fiber dispersion into account can be found in the recent review [16].

A recent extensive experimental study has revealed that the collagen fiber distribution in layers of healthy human abdominal and thoracic aortas, and iliac arteries is not exactly symmetric about one particular direction – the out-of-plane fiber dispersion is in general much smaller than the in-plane dispersion [5] – in contrast to the assumption of symmetric fiber dispersion for such tissues [15]. Recently, our group has further extended the GST-based fiber dispersion model [15] to a more general case so that the experimentally observed non-symmetric distribution of fibers can also be captured [16].

It is often assumed that collagen fibers do not contribute to the total strain energy of the material when loaded in compression due to their waviness and slenderness, for example. However, modeling of this phenomenon for computational implementation has been called into question in [17]. In some models a Heaviside step function or similar approaches have been introduced in the AI formulation so as to exclude the strain energy of the compressed fibers; see, e.g., [18–20]. This approach can theoretically eliminate the contribution of the fibers under compression from the total strain energy. But, the numerical integrations over a subdomain of a unit sphere needed for evaluation of the Cauchy stress and elasticity tensors require the integrand to be a continuous function over the integration domain. The presence of the Heaviside step function in the strain-energy function renders the stress and elasticity tensors discontinuous over the unit sphere, as indicated in [19]. A recent study [4] proposed to approximate the integration for the Cauchy stress tensor by a symmetric cubature formula with a finite number of integration points and weights over the unit sphere [21], with each integration point representing a spatial

fiber orientation on the sphere. In this approach, if the collagen fiber at an integration point is compressed, then the strain energy of that fiber orientation is eliminated from the numerical integration. This leads to a discontinuous strain-energy function over the unit sphere whereas the cubature formula, as described in [21], requires continuous functions. Thus, a finite element implementation of this method is not likely to be accurate for the computation of the stress and elasticity tensors, and leads to a poor rate of convergence.

In order to obtain a continuous stress response and strain-energy function, an *equivalent* transversely isotropic deformation state defined by using the squared stretch in the mean fiber direction and an average squared stretch of all fibers in the plane transverse to the mean fiber direction was proposed recently [22] in order to eliminate the contribution of compressed fibers. However, as the authors pointed out, if both squared stretches are greater than 1, then no fiber would be excluded with this method. Indeed, for simple shear, e.g., it is very easy to show that their criterion for including just the extended fibers does not exclude all the compressed fibers, and this limitation also applies to other deformations.

To completely exclude the fibers under compression for any deformation state, we have developed a modified fiber dispersion model [17] based on the AI approach. This model incorporates a weighted strain-energy function and enables the Cauchy stress and elasticity tensors to be evaluated in a straightforward way. In addition, we have also discussed the integration boundary of the region that admits only extended fibers under any deformation state [23], implemented this model in the finite element analysis program FEAP [24] and verified it with several numerical examples. However, in that study, for purposes of illustration of the method, we demonstrated the new fiber dispersion model [17] by using a simple quadratic form of strain-energy function, namely the standard fiber-reinforcing model [25], for the fiber contribution. However, the quadratic form of the strain-energy function is not able to capture the highly nonlinear mechanical response of some soft biological tissues such as arterial tissues, and an exponential form of the strain-energy function is more suitable for those tissues [15, 26]. This can be verified by fitting the constitutive law documented in [23], which is based on the standard fiber-reinforcing model, to experimental data of of arterial tissue. It is impossible to accurately fit the highly nonlinear behavior of soft tissues, like the one in Section 3.3, by using the quadratic strain-energy function for fibers. Therefore, the goal of this study is to further develop the new model by using an exponential form of strain-energy function for collagen fibers and to illustrate the application of the model to some representative numerical examples, including the extension–inflation simulation of a residually stressed carotid artery.

The present study is structured as follows. In Section 2 we present the continuum mechani-

cal framework of the proposed constitutive model with exclusion of compressed fibers from the total strain energy in a decoupled form suitable for computational implementation, including the expressions of Cauchy stress and the elasticity tensors for 3D fiber distribution. In Section 3 the theory of Section 2 is applied to several representative examples by using the finite element based numerical integration scheme from [23]. In particular, three numerical simulations are presented with the goal of demonstrating the efficacy of the proposed constitutive model and its computational implementation. Finally, Section 4 summarizes the proposed constitutive modeling approach and discusses possible future studies of the present work.

2 Continuum Mechanical Framework

In this section, we present briefly the notation and fundamental elements of nonlinear continuum mechanics in order to describe the fiber dispersion model. Then, the corresponding Cauchy stress and fourth-order elasticity tensors needed for finite element implementation are also discussed.

2.1 Kinematics

Let $\mathcal{B}_0$ be a reference configuration of a continuum body which is stress free and $\mathcal{B}$ its deformed configuration. The deformation map $\mathbf{x} = \boldsymbol{\chi}(\mathbf{X})$ transforms a material point $\mathbf{X} \in \mathcal{B}_0$ into a spatial point $\mathbf{x} \in \mathcal{B}$. From this deformation map we derive the deformation gradient $\mathbf{F}(\mathbf{X}) = \partial\boldsymbol{\chi}(\mathbf{X})/\partial\mathbf{X}$ and its determinant $J = \det\mathbf{F}(\mathbf{X})$, where J is the local volume ratio; we require $J > 0$.

Following the multiplicative decomposition of the deformation gradient in [27, 28] we decouple $\mathbf{F}$ into a spherical (dilatational) part $J^{1/3}\mathbf{I}$ and a unimodular (distortional) part $\overline{\mathbf{F}} = J^{-1/3}\mathbf{F}$, with $\det\overline{\mathbf{F}} \equiv 1$. We define the right Cauchy–Green tensor $\mathbf{C} = \mathbf{F}^{\mathrm{T}}\mathbf{F}$ and its modified counterpart $\overline{\mathbf{C}} = \overline{\mathbf{F}}^{\mathrm{T}}\overline{\mathbf{F}}$, respectively, with the related invariants $I_1 = \mathrm{tr}\mathbf{C}$ and $\bar{I}_1 = \mathrm{tr}\overline{\mathbf{C}}$.

2.2 Fiber Dispersion Model

In general, we can treat each layer of an arterial wall as an incompressible, elastic and fiber-reinforced continuum body embedded with a 3D dispersed fiber distribution. Collagen fibers may be rotationally symmetrically or non-symmetrically dispersed about a mean orientation in the 3D space [16]. Since our main focus here is to examine the effect of excluding compressed fibers, for purposes of illustration we adopt a rotationally symmetric dispersion of fibers. To

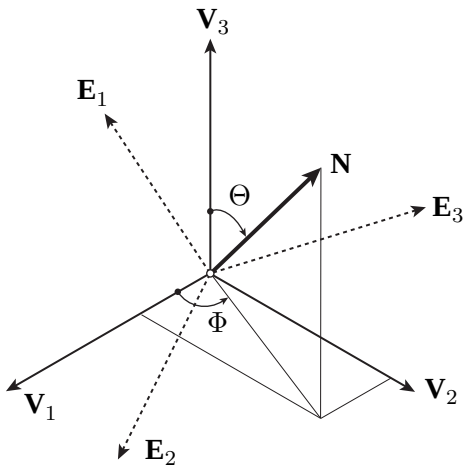

Figure 1: Unit vector **N** representing an arbitrary fiber direction described in a local coordinate system constructed from the eigenvectors $\mathbf{V}_i$, $i = 1, 2, 3$, of **C**. The components of **N** in terms of the global Cartesian basis vectors $\mathbf{E}_i$, $i = 1, 2, 3$, can be calculated by a rotation tensor **R** such that $\mathbf{V}_i = \mathbf{R}\mathbf{E}_i$, $i = 1, 2, 3$.

eliminate the fibers under compression for a general deformation state, we have proposed a modified fiber dispersion model [17] based on the AI approach.

Briefly, an arbitrary fiber direction **N** from the center of a unit sphere can be described by two spherical polar angles (Θ, Φ) as

$$\mathbf{N} = \sin\Theta\cos\Phi\mathbf{V}_1 + \sin\Theta\sin\Phi\mathbf{V}_2 + \cos\Theta\mathbf{V}_3, \tag{1}$$

where $\mathbf{V}_i$, $i = 1, 2, 3$, are the unit eigenvectors of **C**. For a given **C**, the triad $\{\mathbf{V}_1, \mathbf{V}_2, \mathbf{V}_3\}$, namely the so-called Lagrangian axes at point $\mathbf{X} \in \mathcal{B}_0$ in the reference configuration [29], defines a unique local coordinate system, as shown in Figure 1. The two spherical polar angles have the ranges $\Theta \in [0, \pi]$ and $\Phi \in [-\pi/2, \pi/2]$, which define a half sphere, denoted $\mathbb{S}$. We only consider a half sphere since **N** and $-\mathbf{N}$ represent the same fiber. In (1), the vector **N** is decomposed on the local coordinate system instead of the global Cartesian basis vectors because this makes it more convenient to describe the boundary of the integration domain within which fibers are extended, as explained in [23]. The fiber orientation **N** can also be described in terms of the Cartesian basis vectors $\mathbf{E}_i$, $i = 1, 2, 3$, in a global coordinate system. The eigenvectors of **C** can be expressed as $\mathbf{V}_i = \mathbf{R}\mathbf{E}_i$, $i = 1, 2, 3$, where **R** is a rotation tensor (which depends on **C**).

Analogously to (1), we can write the mean fiber direction, denoted **M**, as

$$\mathbf{M} = \sin\Theta_{\mathrm{M}}\cos\Phi_{\mathrm{M}}\mathbf{V}_1 + \sin\Theta_{\mathrm{M}}\sin\Phi_{\mathrm{M}}\mathbf{V}_2 + \cos\Theta_{\mathrm{M}}\mathbf{V}_3, \tag{2}$$

where Θ_{M} and Φ_{M} can be determined by using the relations

$$\cos\Theta_{\mathrm{M}} = \mathbf{V}_3 \cdot \mathbf{M}, \qquad \tan\Phi_{\mathrm{M}} = \frac{\mathbf{V}_2 \cdot \mathbf{M}}{\mathbf{V}_1 \cdot \mathbf{M}}. \tag{3}$$

Note that $\mathbf{M}$ is a given constant unit vector in the reference configuration, but Θ_{M} and Φ_{M} depend on $\mathbf{C}$ through (3).

In this study, since we consider the soft tissue as an elastic material, it is assumed that there exists a strain-energy function $\Psi(\mathbf{C}, \{\mathbf{N}\})$ which depends on the macroscopic deformation of the material through $\mathbf{C}$, the underlying fiber through each direction $\mathbf{N}$, and a PDF $\rho(\Theta, \Phi)$ that describes the distribution of fibers in 3D space. Note that the notation $\{\mathbf{N}\}$ indicates the dependence on the distribution of $\mathbf{N}$ in space. The PDF satisfies the normalization condition

$$\frac{1}{2\pi} \iint_{\mathbb{S}} \rho(\Theta, \Phi) \sin\Theta \, \mathrm{d}\Theta \, \mathrm{d}\Phi = 1. \tag{4}$$

Specifically, for a rotationally symmetric fiber dispersion, $\rho(\Theta, \Phi)$ is a function of the angle between $\mathbf{N}$ and the mean fiber direction $\mathbf{M}$. The PDF should be determined by experimental data of the 3D fiber distribution in the specific layers of the biological tissue.

For computational purposes [33], we assume that the strain-energy function can be decoupled as [30]

$$\Psi(\mathbf{C}, \{\mathbf{N}\}) = \Psi_{\mathrm{vol}}(J) + \Psi_{\mathrm{iso}}(\overline{\mathbf{C}}, \{\mathbf{N}\}), \tag{5}$$

where the function Ψ_{vol} represents the energy contribution by a purely volumetric deformation while Ψ_{iso} represents the contribution from an isochoric (volume preserving) deformation through $\overline{\mathbf{C}}$. It is assumed that the isochoric strain energy Ψ_{iso} is the superposition of the energy contributions from the (non-collagenous) ground substance Ψ_{g} and the fibers Ψ_{f}, i.e.

$$\Psi_{\mathrm{iso}} = \Psi_{\mathrm{g}}(\overline{\mathbf{C}}) + \Psi_{\mathrm{f}}(\overline{\mathbf{C}}, \{\mathbf{N}\}). \tag{6}$$

Following [17, 26] we treat the ground substance as a neo-Hookean material in terms of $\bar{I}_1$ as $\Psi_{\mathrm{g}}(\bar{I}_1) = \mu(\bar{I}_1 - 3)/2$, where the parameter μ is the shear modulus of the ground substance in the reference configuration. Similarly to [15, 23], we assume that the isochoric part of the strain energy per unit reference volume associated with the fibers in the direction $\mathbf{N}$ is a function of $\bar{I}_4$. Unlike in [23], in which the standard fiber-reinforcing model [25] was adopted for the fiber contributions, for highly nonlinear deformations an exponential form of the strain-energy function is more suitable. Thus, following [26], the strain energy of all the fibers orientated in the direction $\mathbf{N}$ per unit reference volume now becomes

$$\Psi_{\mathrm{n}}(\bar{I}_4) = \frac{k_1}{2k_2} \left(\mathrm{e}^{k_2(\bar{I}_4 - 1)^2} - 1 \right), \tag{7}$$

where k_1 is a positive material parameter with the dimension of stress, k_2 is a positive dimensionless material parameter and $\bar{I}_4(\mathbf{N}) = \overline{\mathbf{C}} : \mathbf{N} \otimes \mathbf{N} = J^{-2/3} I_4(\mathbf{N})$, while the invariant $I_4(\mathbf{N})$ is the squared fiber stretch in the direction $\mathbf{N}$; see, e.g., [30]. By using (1), $I_4(\mathbf{N})$ is then expressed in terms of the eigenvectors of $\mathbf{C}$ as

$$\begin{aligned} I_4(\mathbf{N}) = \mathbf{C} : \mathbf{N} \otimes \mathbf{N} = \cos^2\Theta \mathbf{V}_3 \cdot (\mathbf{C}\mathbf{V}_3) + \sin^2\Theta \left[\cos^2\Phi \mathbf{V}_1 \cdot (\mathbf{C}\mathbf{V}_1) + \sin^2\Phi \mathbf{V}_2 \cdot (\mathbf{C}\mathbf{V}_2)\right] \\ + 2\sin\Theta\cos\Theta(\cos\Phi\mathbf{V}_1 + \sin\Phi\mathbf{V}_2) \cdot (\mathbf{C}\mathbf{V}_3) + 2\sin^2\Theta\sin\Phi\cos\Phi\mathbf{V}_1 \cdot (\mathbf{C}\mathbf{V}_2). \end{aligned} \tag{8}$$

With respect to its eigenvectors, $\mathbf{C}$ has the spectral decomposition

$$\mathbf{C} = \lambda_1^2 \mathbf{V}_1 \otimes \mathbf{V}_1 + \lambda_2^2 \mathbf{V}_2 \otimes \mathbf{V}_2 + \lambda_3^2 \mathbf{V}_3 \otimes \mathbf{V}_3, \tag{9}$$

where the squared principal stretches λ_i^2, $i = 1, 2, 3$, are the eigenvalues of $\mathbf{C}$. Then I_4 can be expressed as [17]

$$I_4(\Theta, \Phi) = \sin^2\Theta(\lambda_1^2\cos^2\Phi + \lambda_2^2\sin^2\Phi) + \lambda_3^2\cos^2\Theta. \tag{10}$$

Hence, the strain energy Ψ_{f} due to all the extended fibers per unit reference volume is given by

$$\Psi_{\mathrm{f}} = \frac{1}{2\pi} \iint_{\Omega} \rho(\Theta, \Phi) \Psi_{\mathrm{n}}(\bar{I}_4(\Theta, \Phi)) \sin\Theta \, \mathrm{d}\Theta \, \mathrm{d}\Phi, \tag{11}$$

where $\Omega = \{(\Theta, \Phi) \in \mathbb{S} \mid I_4(\Theta, \Phi) > 1\}$ which defines the deformation dependent domain in which fibers are extended. Note that Ψ_{n} here incorporates the factor n used previously in [31] to represent the number of fibers per unit reference volume.

The total isochoric strain-energy function due to the ground substance and the collagen fibers now reads

$$\Psi_{\mathrm{iso}} = \Psi_{\mathrm{g}}(\bar{I}_1) + \frac{1}{2\pi} \iint_{\Omega} \rho(\Theta, \Phi) \Psi_{\mathrm{n}}(\bar{I}_4(\Theta, \Phi)) \sin\Theta \, \mathrm{d}\Theta \, \mathrm{d}\Phi. \tag{12}$$

For the layers of an arterial wall with two or more families of fibers, the strain energy associated with additional fiber families can be added to (12), as in the numerical example in Section 3.3.

2.2.1 Stress Tensor

Differentiation of the strain-energy function (5) with respect to $\mathbf{C}$ yields the second Piola–Kirchhoff stress tensor $\mathbf{S} = 2\partial\Psi/\partial\mathbf{C}$. We identify two stress contributions, $\mathbf{S}_{\mathrm{vol}}$ and $\mathbf{S}_{\mathrm{iso}}$ with $\mathbf{S} = \mathbf{S}_{\mathrm{vol}} + \mathbf{S}_{\mathrm{iso}}$, from the decoupled form of Ψ. Since the volumetric contribution $\mathbf{S}_{\mathrm{vol}}$ for hyperelastic material models has been extensively documented and implemented in finite element

programs, see [30], here we focus only on the isochoric part, i.e.

$$\mathbf{S}_{\text{iso}} = J^{-2/3}\mathbb{P} : \overline{\mathbf{S}}, \qquad \overline{\mathbf{S}} = 2\frac{\partial \Psi_{\text{iso}}}{\partial \overline{\mathbf{C}}}, \tag{13}$$

where $\overline{\mathbf{S}}$ defines the so-called fictitious isochoric second Piola–Kirchhoff stress tensor [30], $\mathbb{P} = \mathbb{I} - \frac{1}{3}\mathbf{C}^{-1} \otimes \mathbf{C}$ is a fourth–order Lagrangian projection tensor, $\mathbb{I}$ being the symmetric fourth-order unit tensor with components $(\mathbb{I})_{ABCD} = \frac{1}{2}(\delta_{AC}\delta_{BD} + \delta_{AD}\delta_{BC})$. From (12) and $(13)_2$ we obtain

$$\overline{\mathbf{S}} = 2\psi_{\text{g}}'(\bar{I}_1)\mathbf{I} + \frac{1}{\pi}\iint\limits_{\Omega} \rho(\Theta,\Phi)\psi_{\text{n}}'\left(\bar{I}_4(\Theta,\Phi)\right)\sin\Theta\, \mathbf{N}\otimes\mathbf{N}\,\mathrm{d}\Theta\,\mathrm{d}\Phi, \tag{14}$$

where $\mathbf{I}$ is the second-order identity tensor, $\psi_{\text{g}}'(\bar{I}_1) = \partial\Psi_{\text{g}}(\bar{I}_1)/\partial\bar{I}_1$, and $\psi_{\text{n}}' = \partial\Psi_{\text{n}}(\bar{I}_4)/\partial\bar{I}_4$. Substituting (14) into $(13)_1$ we obtain the isochoric second Piola–Kirchhoff stress tensor $\mathbf{S}_{\text{iso}}$. Since the boundary of the integration domain Ω in (12) depends on $\mathbf{C}$, the derivative of Ψ_{iso} with respect to $\mathbf{C}$ should, in general, include an integral over the boundary of Ω. This integral vanishes since Ψ_{n} vanishes on the boundary for incompressible materials. A simple derivation of the integral in (14) based on the general Leibniz integral rule using (12) and (13) is given in Appendix A.

The Cauchy stress tensor $\boldsymbol{\sigma} = J^{-1}\mathbf{F}\mathbf{S}\mathbf{F}^{\text{T}}$ is obtained by a push forward of the second Piola–Kirchhoff stress tensor $\mathbf{S}$. The isochoric part $\boldsymbol{\sigma}_{\text{iso}}$ of the Cauchy stress tensor can be calculated via the fictitious form $\overline{\boldsymbol{\sigma}}$ by

$$\boldsymbol{\sigma}_{\text{iso}} = \mathbb{P} : \overline{\boldsymbol{\sigma}}, \tag{15}$$

where $\mathbb{P} = \mathbb{I} - \frac{1}{3}\mathbf{I}\otimes\mathbf{I}$ is the fourth–order Eulerian projection tensor [30], $\mathbb{I}$ being the symmetric fourth–order unit tensor with components $(\mathbb{I})_{abcd} = \frac{1}{2}(\delta_{ac}\delta_{bd} + \delta_{ad}\delta_{bc})$, and the fictitious Cauchy stress tensor $\overline{\boldsymbol{\sigma}}$ is defined by

$$\overline{\boldsymbol{\sigma}} = J^{-1}\overline{\mathbf{F}}\,\overline{\mathbf{S}}\,\overline{\mathbf{F}}^{\text{T}} = J^{-1}[2\psi_{\text{g}}'\overline{\mathbf{b}} + \frac{1}{\pi}\iint\limits_{\Omega} \rho(\Theta,\Phi)\psi_{\text{n}}'\left(\bar{I}_4(\Theta,\Phi)\right)\sin\Theta\,\overline{\mathbf{n}}\otimes\overline{\mathbf{n}}\,\mathrm{d}\Theta\,\mathrm{d}\Phi], \tag{16}$$

where $\overline{\mathbf{b}} = \overline{\mathbf{F}}\,\overline{\mathbf{F}}^{\text{T}}$ is the modified left Cauchy–Green tensor, and $\overline{\mathbf{n}} = \overline{\mathbf{F}}\mathbf{N}$.

2.2.2 Elasticity Tensor

Similarly to the decoupled forms of the stress tensors, the decoupled form of the elasticity tensor $\mathbb{C}$ in the Lagrangian description is given by ([30], p. 254)

$$\mathbb{C} = \mathbb{C}_{\text{vol}} + \mathbb{C}_{\text{iso}}. \tag{17}$$

Since the volumetric part $\mathbb{C}_{\text{vol}}$ of the elasticity tensor $\mathbb{C}$ has been well documented, in this study we again focus our attention on the isochoric part [30], i.e.

$$\mathbb{C}_{\text{iso}} = 2\frac{\partial \mathbf{S}_{\text{iso}}}{\partial \mathbf{C}}, \tag{18}$$

which, as given in [30], p. 255, depends on the fourth-order fictitious elasticity tensor $\overline{\mathbb{C}}$ in the Lagrangian description, i.e.

$$\overline{\mathbb{C}} = 2J^{-4/3}\frac{\partial \overline{\mathbf{S}}}{\partial \overline{\mathbf{C}}} = 2J^{-4/3}\frac{\partial \overline{\mathbf{S}}}{\partial \bar{I}_1} \otimes \mathbf{I} + 2J^{-4/3}\frac{\partial \overline{\mathbf{S}}}{\partial \bar{I}_4} \otimes \mathbf{N} \otimes \mathbf{N}. \tag{19}$$

By using the expression for $\overline{\mathbf{S}}$ from (14) in (19) we obtain

$$\overline{\mathbb{C}} = 4J^{-4/3}\psi''_{\text{g}}(\bar{I}_1)\mathbf{I}\otimes\mathbf{I} + J^{-4/3}\frac{2}{\pi}\iint\limits_{\Omega} \rho(\Theta,\Phi)\psi''_{\text{n}}\left(\bar{I}_4(\Theta,\Phi)\right)\ \mathbf{N}\otimes\mathbf{N}\otimes\mathbf{N}\otimes\mathbf{N}\sin\Theta \text{d}\Theta\text{d}\Phi, \tag{20}$$

where

$$\psi''_{\text{g}}(\bar{I}_1) = \frac{\partial^2 \Psi_{\text{g}}(\bar{I}_1)}{\partial \bar{I}_1 \partial \bar{I}_1}, \qquad \psi''_{\text{n}}\left(\bar{I}_4(\Theta,\Phi)\right) = \frac{\partial^2 \Psi_{\text{n}}\left(\bar{I}_4(\Theta,\Phi)\right)}{\partial \bar{I}_4 \partial \bar{I}_4}. \tag{21}$$

Similarly to the derivation of (14) the integral over the boundary of Ω obtained by differentiating (14) with respect to $\overline{\mathbf{C}}$ is omitted from (20); see Appendix A.

With the neo-Hookean model for the ground substance and the exponential model (7) for the fibers, the fictitious elasticity tensor becomes

$$\overline{\mathbb{C}} = J^{-4/3}\frac{2k_1}{\pi}\iint\limits_{\Omega} \rho(\Theta,\Phi)\left[1 + 2k_2(\bar{I}_4 - 1)^2\right] \text{e}^{k_2(\bar{I}_4-1)^2}\mathbf{N}\otimes\mathbf{N}\otimes\mathbf{N}\otimes\mathbf{N}\sin\Theta\,\text{d}\Theta\,\text{d}\Phi, \tag{22}$$

and a push-forward operation on $\overline{\mathbb{C}}$ with $\mathbf{F}$ yields the Eulerian form of the fictitious elasticity tensor, i.e.

$$\overline{\mathbb{c}} = \frac{2k_1}{\pi}\iint\limits_{\Omega} \rho(\Theta,\Phi)\left[1 + 2k_2(\bar{I}_4 - 1)^2\right] \text{e}^{k_2(\bar{I}_4-1)^2}\overline{\mathbf{n}}\otimes\overline{\mathbf{n}}\otimes\overline{\mathbf{n}}\otimes\overline{\mathbf{n}}\sin\Theta\,\text{d}\Theta\,\text{d}\Phi. \tag{23}$$

Note that for the neo-Hookean model $\psi''_{\text{g}}(\bar{I}_1) = 0$. Finally, with (23) we obtain the resulting isochoric part of the elasticity tensor in the Eulerian description, i.e.

$$\mathbb{c}_{\text{iso}} = J^{-1}\mathbb{P} : \bar{\mathbb{C}} : \mathbb{P} + \frac{2}{3}\text{tr}(\bar{\boldsymbol{\sigma}})\mathbb{P} - \frac{2}{3}(\boldsymbol{\sigma}_{\text{iso}}\otimes\mathbf{I} + \mathbf{I}\otimes\boldsymbol{\sigma}_{\text{iso}}), \tag{24}$$

which is required for the computational implementation.

3 Representative Numerical Examples

Similarly to [23], the proposed fiber dispersion model (12) has been implemented in the finite element analysis program FEAP at the integration point level. To illustrate the method, we adopted the von Mises distribution, given by

$$\rho(\Theta,\Phi) = 4\sqrt{\frac{b}{2\pi}}\frac{\exp[2b(\mathbf{N}\cdot\mathbf{M})^2]}{\mathrm{erfi}(\sqrt{2b})}, \tag{25}$$

as the PDF for the 3D fiber dispersion in the computational implementation, where the constant b is a concentration parameter describing how closely the fibers are distributed around the mean direction and $\mathrm{erfi}(x) = -\mathrm{i}\ \mathrm{erf}(\mathrm{i}\ x)$ denotes the imaginary error function in which the error function $\mathrm{erf}(x)$ is defined by

$$\mathrm{erf}(x) = \frac{2}{\sqrt{\pi}}\int_0^x \exp(-\xi^2)\mathrm{d}\xi. \tag{26}$$

On substituting (25) into the isochoric Cauchy stress tensor (15) and the Eulerian fourth–order fictitious elasticity tensor (23), respectively, the specific forms of the Cauchy stress and Eulerian elasticity tensors may be obtained. Then, similarly to [23], we have adopted a finite element based numerical integration scheme for evaluation of the double integrals in the Cauchy stress and elasticity tensors.

In this section we demonstrate the performance and computational implementation of the fiber dispersion model (12) by means of three representative numerical examples, specifically uniaxial extension and simple shear of a unit cube with a 3D fiber dispersion, and an extension–inflation simulation of a residually stressed carotid artery. For each example we have assumed an *incompressible* hyperelastic material. The augmented Lagrangian method in FEAP was adopted to enforce incompressibility [32]. In each example, the 3D geometry of the model was discretized with 8–node hexahedral mixed Q1/P0 elements, and the problems were solved by using the Newton–Raphson method. The finite element results are verified with experimental data or analytical solutions obtained by using either MATLAB [34] or MATHEMATICA [35].

3.1 Uniaxial Extension

As our first example we consider a uniaxial extension test of a unit cube composed of one hexahedral element in the mean fiber direction by using the fiber dispersion model (12). The geometry of the cube is $1\times1\times1$ mm aligned with the Cartesian axes $\mathbf{E}_1$, $\mathbf{E}_2$ and $\mathbf{E}_3$. We assume

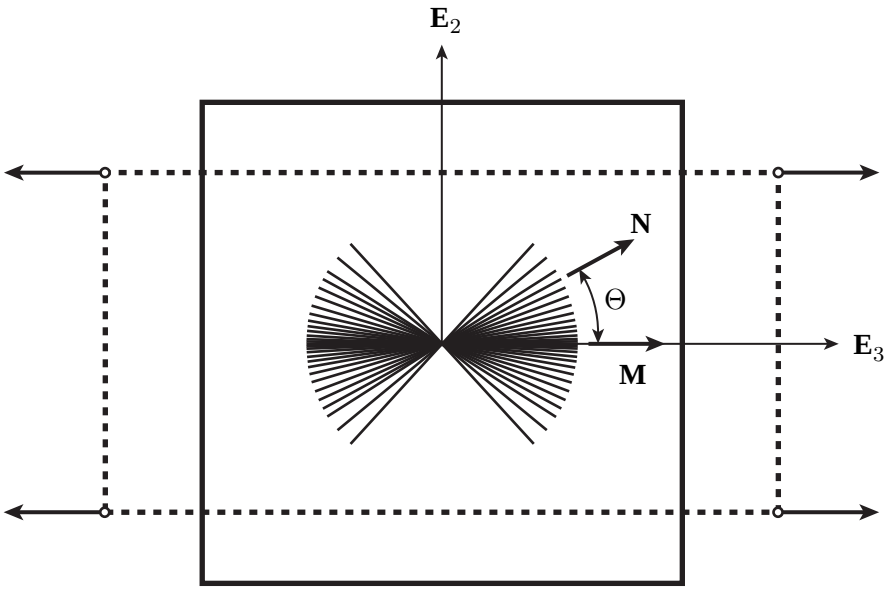

Figure 2: Cross-section of a unit cubic containing a rotationally symmetric fiber dispersion with the mean fiber direction **M** aligned with the loading direction $\mathbf{E}_3$. An arbitrary fiber orientation within the dispersion is denoted by **N**. The dashed lines show the deformed configuration of the cross-section.

one family of fibers with rotationally symmetric dispersion about the mean fiber direction $\mathbf{M} = \mathbf{E}_3$, as depicted in Figure 2. The model is subjected to unconfined uniaxial extension in the $\mathbf{E}_3$ direction such that the deformation is homogeneous. Because the material is incompressible, the matrix forms of the deformation gradient and the Cauchy–Green tensors are

$$[\mathbf{F}] = \mathrm{diag}[\lambda^{-1/2}, \lambda^{-1/2}, \lambda], \qquad [\mathbf{b}] = [\mathbf{C}] = \mathrm{diag}[\lambda^{-1}, \lambda^{-1}, \lambda^2], \tag{27}$$

where λ is the stretch in the $\mathbf{E}_3$ direction. For this special case the Cartesian basis vectors $\mathbf{E}_1 = \mathbf{V}_2, \mathbf{E}_2 = \mathbf{V}_3, \mathbf{E}_3 = \mathbf{V}_1$, are the eigenvectors of **C**. For any fiber direction **N** within the half sphere, $I_4(\Theta, \Phi)$ is then given by

$$I_4(\Theta) = \lambda^{-1} \sin^2 \Theta + \lambda^2 \cos^2 \Theta, \tag{28}$$

which is independent of Φ.

Consider the decoupled form of the fictitious Cauchy stress tensor (16) and the isochoric Cauchy stress tensor (15), which is based on (16), so that the corresponding Cauchy stress tensor $\boldsymbol{\sigma}$ for an incompressible material is

$$\boldsymbol{\sigma} = -p\mathbf{I} + \mu\mathbf{b} + \frac{k_1}{\pi} \iint_{\Omega} \rho(\Theta, \Phi) \mathrm{e}^{k_2 (I_4 - 1)^2} \, (I_4 - 1) \sin \Theta \, \mathbf{n} \otimes \mathbf{n} \, \mathrm{d}\Theta \, \mathrm{d}\Phi, \tag{29}$$

where for this special case $\Omega = \{(\Theta, \Phi) \mid \Theta \in [0, \pi/2], \Phi \in [0, 2\pi], I_4(\Theta, \Phi) > 1\}$, $\rho(\Theta, \Phi)$ reduces to $\rho(\Theta)$, p is a Lagrange multiplier, and $\mathbf{n} = \mathbf{FN}$. The tensor product $\mathbf{n} \otimes \mathbf{n}$ can be expanded as in [23]. Thus, the Cauchy stress $\sigma \equiv \sigma_{33}$ in the $\mathbf{E}_3$ direction is

$$\sigma = -p + (\mu + \alpha)\lambda^2, \tag{30}$$

where α is defined as

$$\alpha = 2k_1 \int_{\Sigma} \rho(\Theta) \mathrm{e}^{k_2(I_4(\Theta)-1)^2} (I_4(\Theta) - 1) \sin\Theta \cos^2\Theta \, \mathrm{d}\Theta, \tag{31}$$

with $\Sigma = \{\Theta \in [0, \pi/2] \mid I_4 > 1\}$, and the PDF ρ in (25) specializes to

$$\rho(\Theta) = 4\sqrt{\frac{b}{2\pi}} \frac{\exp(2b\cos^2\Theta)}{\operatorname{erfi}(\sqrt{2b})}. \tag{32}$$

Since we are considering uniaxial extension $\sigma_{11} = \sigma_{22} = 0$, the Lagrange multiplier is $p = (\mu + \beta)\lambda^{-1}$, where

$$\beta = k_1 \int_{\Sigma} \rho(\Theta) \mathrm{e}^{(k_2(I_4(\Theta)-1)^2)} (I_4(\Theta) - 1) \sin^3\Theta \, \mathrm{d}\Theta, \tag{33}$$

and hence, on elimination of p, the uniaxial Cauchy stress σ becomes

$$\sigma = (\mu + \alpha)\lambda^2 - (\mu + \beta)\lambda^{-1}. \tag{34}$$

We have implemented this analytical solution in MATLAB and adopted the adaptive Gauss–Kronrod quadrature method (`quadgk`) for the integrations of the coefficients α and β using (28). For comparison between the finite element results obtained with FEAP and the analytical solution obtained with MATLAB, we have adopted the following material parameters $\mu = 1.64\,\text{kPa}$, $b = 0.01$, $k_1 = 5.63\,\text{kPa}$ and $k_2 = 14.25$. This set of parameters was chosen to highlight the capability of the fiber constitutive equation (7) for modeling highly nonlinear materials responses.

The Cauchy stress versus stretch curves from FEAP and MATLAB are shown in Figure 3. Also shown are the corresponding results for the case in which the coefficients α and β are evaluated numerically over the entire half sphere $\mathbb{S}$ instead of Σ. Thus, the compressed and extended fibers are both accounted for by the second method (dashed curve in Figure 3). As shown, the difference between the two methods increases slightly with an increase in stretch, see the surface plot of $I_4(\Theta, \Phi)$ in Figure 4(a). This difference reduces for larger values of the stretch λ because more fibers are included in the integration domain. Note that the fiber dispersion model was implemented in FEAP based on the eigenvectors of $\mathbf{C}$. The gap shown in

Figure 4(a), which indicates the plane where $I_4 = 1$, expands with increasing stretch according to (28). Figure 4(b) shows the surface plot of the PDF $\rho(\Theta, \Phi)$ from which we can see that there are slightly fewer fibers distributed in the domain where $I_4 \leq 1$, than in the domain where $I_4 > 1$.

3.2 Simple Shear

Similarly to Section 3.1, in this example we test the capability of the proposed constitutive model by subjecting the same unit cube ($1 \times 1 \times 1\,$mm) to a simple shear deformation. All the nodes on the bottom face of the cube in the $(\mathbf{E}_1, \mathbf{E}_2)$-plane are constrained in all three translational degrees of freedom, see Figure 5, and a horizontal displacement in the $\mathbf{E}_1$ direction is applied on the top face. The mean fiber direction $\mathbf{M}$ is assumed to be oriented at 135° from the $\mathbf{E}_3$ direction in the $(\mathbf{E}_1, \mathbf{E}_3)$-plane in the reference configuration, as illustrated in Figure 5. Thus, the matrix forms of the deformation gradient and the right Cauchy–Green tensor are

$$[\mathbf{F}] = \begin{bmatrix} 1 & 0 & c \\ 0 & 1 & 0 \\ 0 & 0 & 1 \end{bmatrix}, \qquad [\mathbf{C}] = \begin{bmatrix} 1 & 0 & c \\ 0 & 1 & 0 \\ c & 0 & (1+c^2) \end{bmatrix}. \tag{35}$$

Similarly to Section 3.1, for this particular example we can represent an arbitrary fiber orientation $\mathbf{N}$ with respect to the Cartesian basis vectors $\mathbf{E}_i$, $i = 1, 2, 3$, as

$$\mathbf{N} = \sin\Theta\cos\Phi\mathbf{E}_1 + \sin\Theta\sin\Phi\mathbf{E}_2 + \cos\Theta\mathbf{E}_3. \tag{36}$$

Then, the invariant $I_4(\mathbf{N})$ becomes

$$I_4 = 1 + c^2\cos^2\Theta + c\sin 2\Theta\cos\Phi. \tag{37}$$

In this example c is taken to be positive, so the integration domain Ω is determined by the inequality

$$c\cos^2\Theta + \sin 2\Theta\cos\Phi > 0 \tag{38}$$

within a half sphere defined by $\Theta \in [0, \pi]$ and $\Phi \in [-\pi/2, \pi/2]$. Substituting $\mathbf{n} = \mathbf{FN}$ into the general form of the Cauchy stress tensor (29), we obtain the shear stress in the $(\mathbf{E}_1, \mathbf{E}_3)$-plane as

$$\sigma_{13} = (\mu + \alpha)c + \gamma, \tag{39}$$

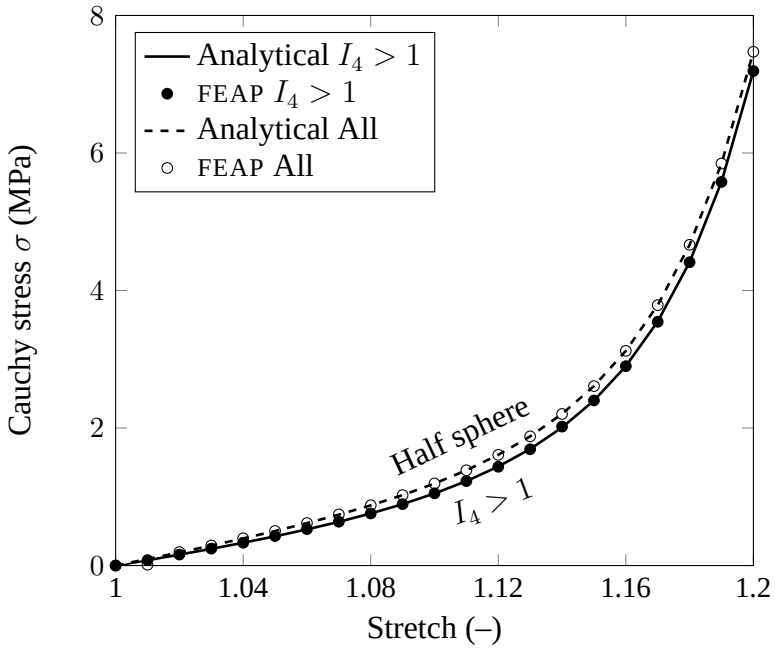

Figure 3: Comparison of the analytical solutions, obtained by using MATLAB, and the numerical results obtained by using FEAP ($\mu = 1.64\,\text{kPa}$, $b = 0.01$, $k_1 = 5.63\,\text{kPa}$, $k_2 = 14.25$). The solid curve is for the case with compressed fibers excluded, and the dashed curve for the case with all the fibers included.

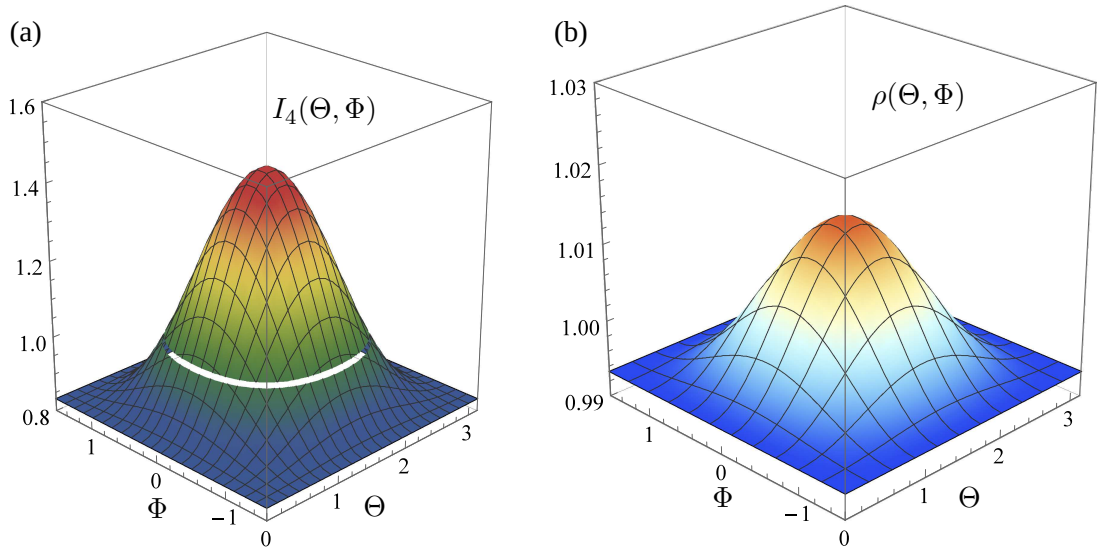

Figure 4: Surface contour plots of (a) $I_4(\Theta, \Phi)$ and (b) $\rho(\Theta, \Phi)$ for a uniaxial tension test within the half sphere $\mathbb{S} = \{(\Theta, \Phi) \mid \Theta \in [0, \pi], \Phi \in [-\pi/2, \pi/2]\}$, defined with respect to a local coordinate system constructed from the eigenvectors of $\mathbf{C}$ ($b = 0.01$, $\lambda = 1.2$). The small gap in (a) represents the plane where $I_4 = 1$. Thus, only the fibers located within the domain enclosed by the gap are extended. In either plot, the center point ($\Theta = \pi/2, \Phi = 0$) represents the mean fiber orientation along the $\mathbf{V}_1$ axis in the local coordinate system, which is coincident with the $\mathbf{E}_3$ axis in the global Cartesian coordinate system; the line at $\Theta = 0$ represents the $\mathbf{V}_3$ axis on the unit sphere; the point located at $\Theta = \pi/2$ and $\Phi = \pi/2$ represents the $\mathbf{V}_2$ axis on the unit sphere.

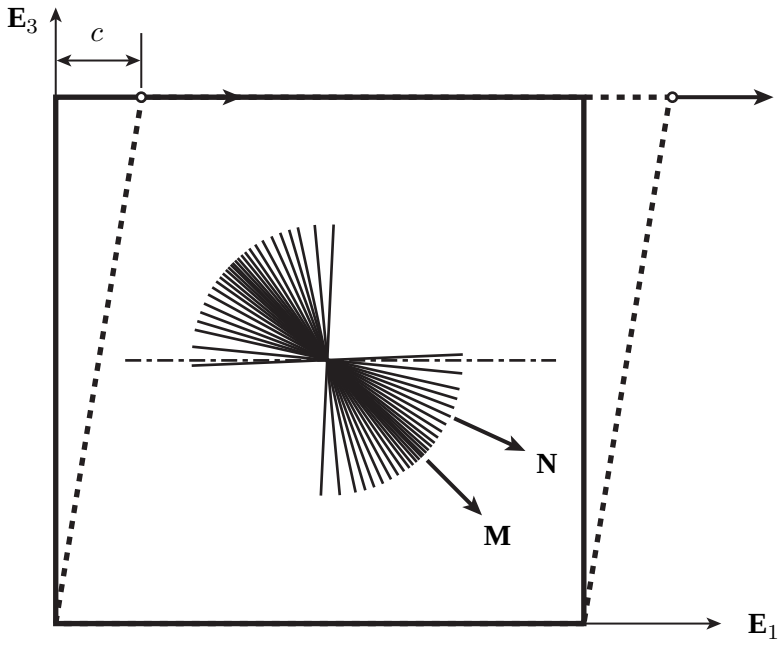

Figure 5: Cross-section of a unit cube subjected to simple shear in the $(\mathbf{E}_1, \mathbf{E}_3)$-plane. The mean fiber direction **M** is aligned at 135° from the $\mathbf{E}_3$ direction in the reference configuration. The fiber dispersion is rotationally symmetric about **M**, and **N** represents a general fiber orientation. The dashed lines show the deformed configuration, where c is the amount of shear.

where α and γ are defined as

$$\begin{aligned}\alpha &= \frac{k_1}{\pi}\iint\limits_{\Omega} \rho(\Theta,\Phi)\mathrm{e}^{(k_2(I_4(\Theta,\Phi)-1)^2)}\,(I_4(\Theta,\Phi)-1)\sin\Theta\cos^2\Theta\,\mathrm{d}\Theta\,\mathrm{d}\Phi,\\ \gamma &= \frac{k_1}{\pi}\iint\limits_{\Omega} \rho(\Theta,\Phi)\mathrm{e}^{(k_2(I_4(\Theta,\Phi)-1)^2)}\,(I_4(\Theta,\Phi)-1)\sin^2\Theta\cos\Theta\cos\Phi\,\mathrm{d}\Theta\,\mathrm{d}\Phi,\end{aligned} \tag{40}$$

and $\Omega = \{(\Theta,\Phi) \in \mathbb{S} \mid I_4 > 1\}$. The normal stresses induced by the simple shear deformation can be determined by the method described in [23]. The coefficients α and γ in (40) should be evaluated in the domain defined by (38), which may be accomplished by using the `NIntegrate` function together with the `Boole` operation in MATHEMATICA. A comparison between the finite element results and the analytical solution obtained by using (39) and MATHEMATICA with the material parameters $\mu = 7.64\,\text{kPa}$, $b = 1.0838$, $k_1 = 996.6\,\text{kPa}$, and $k_2 = 5.249$ is shown in Figure 6. Also shown are the computational and analytical results for the Cauchy shear stress σ_{13} versus the amount of shear c for the case in which the coefficients α and γ are evaluated numerically over the entire half sphere $\mathbb{S}$ instead of Ω.

For this example there is a significant difference between these two cases, which can be explained by the surface plots of I_4 and ρ in Figures 7(a) and (b), respectively, with respect to the

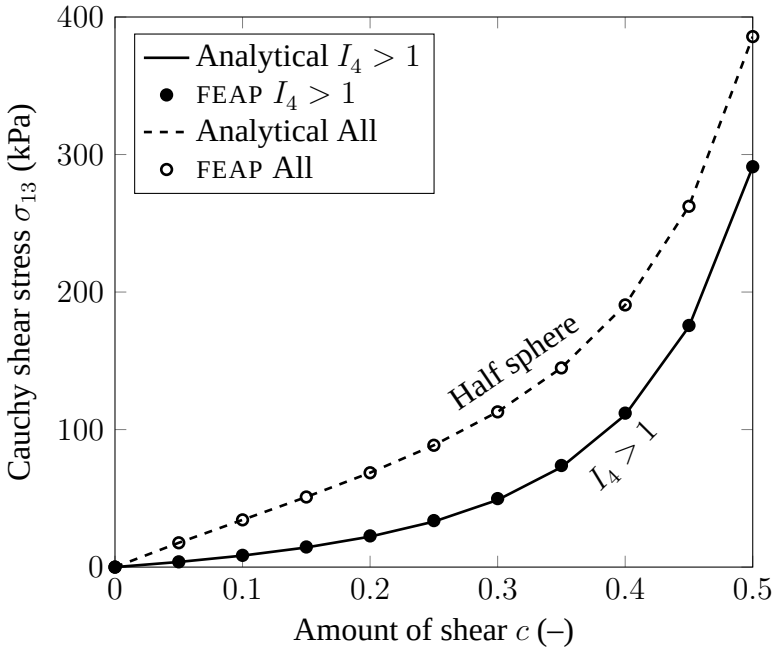

Figure 6: Comparison of the finite element results and the analytical solutions (39) for the simple shear test ($\mu = 7.64\,\text{kPa}$, $b = 1.0838$, $k_1 = 996.6\,\text{kPa}$, $k_2 = 5.249$). The solid curve is for the case with compressed fibers excluded, and the dashed curve for the case with all the fibers included.

local coordinate system. From Figure 7(a), it can be seen that the region where $I_4 < 1$ contains most of the fibers. Thus, by including the contribution from the compressed fibers in the strain-energy function a significantly higher stress response is obtained. A similar observation can be seen in the Figures 7(c) and (d) in which I_4 and ρ, respectively, are plotted with respect to the global Cartesian system. In Figure 6 the significant difference in the values of σ_{13} between the two cases can be seen. This difference gradually disappears with increasing values of c as more fibers are recruited into tension.

3.3 Extension–Inflation of a Residually Stressed Carotid Artery

In this final example, we demonstrate the performance of the fiber dispersion model in a larger problem by simulating an extension–inflation test for a carotid artery with residual stress and two families of fibers accounted for. For purposes of illustration we consider the intact arterial wall as an incompressible, one-layer thick-walled cylindrical tube structure. This approach could be extended to the study of multi-layered arterial tissues given the detailed mechanical properties of each layer from experimental measurements and the fiber orientation and distribution data. It has been shown that residual stresses play an important role in the biomechanics of normal arterial walls [26, 36, 37], especially in terms of homogenizing the circumferential stress

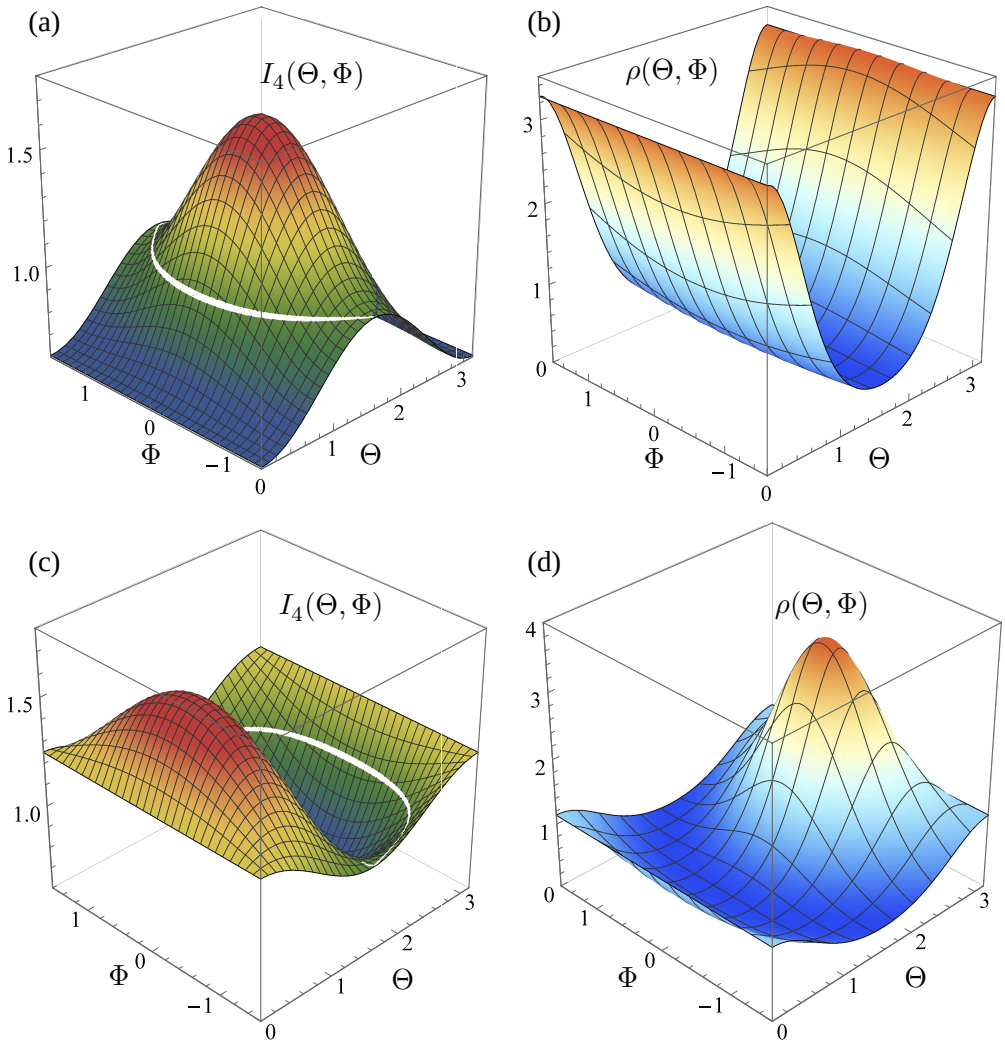

Figure 7: Surface contour plots of (a) $I_4(\Theta, \Phi)$ and (b) $\rho(\Theta, \Phi)$ for a simple shear test within the half sphere $\mathbb{S} = \{(\Theta, \Phi) \mid \Theta \in [0, \pi], \Phi \in [-\pi/2, \pi/2]\}$ defined with respect to a local coordinate system constructed from the eigenvectors of $\mathbf{C}$ ($b = 1.0838$, $c = 0.5$). The small gaps in (a) and (c) represent the plane where $I_4 = 1$. In (a) and (b), the center point ($\Theta = \pi/2, \Phi = 0$) represents the $\mathbf{V}_1$ axis in the local coordinate system; the line at $\Theta = 0$ represents the $\mathbf{V}_3$ axis on the unit sphere; and the point located at $\Theta = \pi/2$ and $\Phi = \pi/2$ represents the $\mathbf{V}_2$ axis on the unit sphere in which the fiber stretch is one. In (c) and (d) I_4 and ρ, respectively, are plotted with respect to the global Cartesian system, which was used for the analytical solution.

through the thickness direction for each layer. We incorporate the residual stress in the arterial model by using the so-called *opening angle method* introduced in [38]. This method assumes the use of the three idealized configurations shown in Figure 8: the load-free configuration in which the artery is excised from the body and not subjected to any load, but is not stress-free;

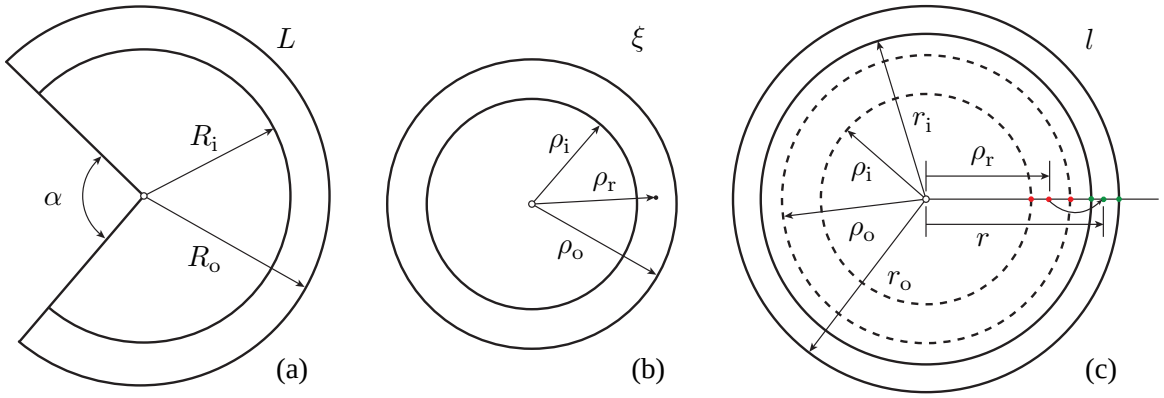

Reference configuration (load-free, stress-free)

Load-free configuration (residually stressed)

Loaded configuration

Figure 8: Kinematics of an arterial wall assumed to be a circular cylindrical tube: cross section at (a) the reference configuration with an opening angle α; (b) the residually stressed load-free configuration; (c) the loaded configuration (due to the applied internal pressure and axial force) compared with the load-free configuration (dashed curves). If no torsion is considered, an arbitrary point at radial location ρ_r transforms to r in the same direction after deformation. The parameters L, ξ and l denote the length of the arterial segments at the three configurations, respectively.

the reference configuration which is stress-free and load-free; and the loaded configuration in which the artery is inflated with an internal pressure and axially stretched by an end force.

To model the extension–inflation of residually stressed artery tissue, the opened sector shown in Figure 8(a) is closed to obtain the residually stressed configuration depicted in Figure 8(b). We then inflate and axially stretch the artery segment simultaneously, as in a typical experiment, see, e.g., [39]. From [39], we obtained the pressure versus circumferential stretch and pressure versus axial stretch curves of human carotid arteries, and we fitted the fiber dispersion model to both curves to obtain the corresponding material parameters. One objective of this example is to predict the internal pressure versus circumferential stretch relation by using pressure versus axial stretch data.

3.3.1 Determination of Material Parameters

The mechanical properties of human common carotid artery tissues have been tested previously by our group [39, 40]. Briefly, carotid artery segment with lengths of about 35 mm were harvested from 11 patients. Two black markers were affixed to the outer surface of the arterial tissue with a distance of about 5 mm. The axial stretch and the outer radius of the arterial speci-

mens were measured between the two markers. During the test, the arterial segment with closed ends was pre-stretched and held at the two ends with the length fixed. Then, an internal pressure was applied on the inner surface of the carotid artery to inflate the specimen. The transmural pressure, axial force, outer diameter, and gage length (distance between the two black markers) were continuously recorded during the pressurization up to $33\,\mathrm{kPa}$. During the entire test, the specimen was immersed in calcium-free saline solution at 37°. It is assumed that there is no torsion during the test.

Thus, the deformation gradient $\mathbf{F}$ and the right Cauchy–Green tensor $\mathbf{C}$ at the outer radius of the specimen have the matrix forms

$$[\mathbf{F}_\mathrm{o}] = \mathrm{diag}[\lambda_{ro}, \lambda_{\theta\mathrm{o}}, \lambda_z], \qquad [\mathbf{C}_\mathrm{o}] = \mathrm{diag}[\lambda_{ro}^2, \lambda_{\theta\mathrm{o}}^2, \lambda_z^2], \tag{41}$$

where $\lambda_{\theta\mathrm{o}}$ is the circumferential stretch determined at the outer radius r_o, λ_z is the axial stretch determined from the gage length, and $\lambda_{ro} = (\lambda_{\theta\mathrm{o}}\lambda_z)^{-1}$ is the radial stretch computed from the incompressibility constraint. Note that here the stretches were measured in the experiment with respect to the load-free configuration. The cylindrical polar basis vectors $\mathbf{E}_R, \mathbf{E}_\Theta, \mathbf{E}_Z$ are the eigenvectors of $\mathbf{C}$, and we note that $\mathbf{E}_R$ and $\mathbf{E}_\Theta$ are functions of position. Thus, for any point within the arterial wall, we can write an arbitrary fiber direction in the reference configuration as

$$\mathbf{N} = \sin\Theta\cos\Phi\mathbf{E}_R + \sin\Theta\sin\Phi\mathbf{E}_\Theta + \cos\Theta\mathbf{E}_Z, \tag{42}$$

and then $I_4(\Theta, \Phi)$ is given by

$$I_4(\Theta, \Phi) = \lambda_{ro}^2\sin^2\Theta\cos^2\Phi + \lambda_{\theta\mathrm{o}}^2\sin^2\Theta\sin^2\Phi + \lambda_z^2\cos^2\Theta. \tag{43}$$

Additionally we assume that the mean fiber directions $\mathbf{M}$ and $\mathbf{M}'$ of the two fiber families in the reference configuration are symmetrically aligned in the tangential plane of the arterial wall so that

$$\mathbf{M} = \cos\Theta_\mathrm{M}\mathbf{E}_\Theta + \sin\Theta_\mathrm{M}\mathbf{E}_Z, \qquad \mathbf{M}' = -\cos\Theta_\mathrm{M}\mathbf{E}_\Theta + \sin\Theta_\mathrm{M}\mathbf{E}_Z, \tag{44}$$

where $\Theta_\mathrm{M} \in [0, \pi/2]$ is the angle between $\mathbf{M}$ and the circumferential direction. From (16) and (15), which is based on (16), we obtained for two families of fibers

$$\boldsymbol{\sigma}_\mathrm{iso} = \mu\overline{\mathbf{b}} + \frac{k_1}{\pi}\sum_{i=4,6}\iint_\Omega \rho_i(\Theta, \Phi)\mathrm{e}^{(k_2(\bar{I}_i-1)^2)}\left(\bar{I}_i - 1\right)\sin\Theta\,\overline{\mathbf{n}}\otimes\overline{\mathbf{n}}\,\mathrm{d}\Theta\,\mathrm{d}\Phi, \tag{45}$$

where the PDFs $\rho_4(\Theta, \Phi)$ and $\rho_6(\Theta, \Phi)$ are defined as

$$\rho_4(\Theta, \Phi) = 4\sqrt{\frac{b}{2\pi}}\frac{\exp[2b(\mathbf{M}\cdot\mathbf{N})^2]}{\mathrm{erfi}(\sqrt{2b})}, \qquad \rho_6(\Theta, \Phi) = 4\sqrt{\frac{b}{2\pi}}\frac{\exp[2b(\mathbf{M}'\cdot\mathbf{N})^2]}{\mathrm{erfi}(\sqrt{2b})}, \tag{46}$$

and by symmetry $\bar{I}_6 = \bar{I}_4$. Following the modeling approach previously established [26, 40], we have the relationship between the internal pressure p_i and the isochoric stress components from the equilibrium equation according to

$$p_\mathrm{i} = \int_{r_\mathrm{i}}^{r_\mathrm{o}} \left(\sigma_{\theta\theta}^{\mathrm{iso}}(r) - \sigma_{rr}^{\mathrm{iso}}(r)\right) \frac{\mathrm{d}r}{r}, \tag{47}$$

where the internal pressure p_i and the deformed outer radius r_o are measured from the experiment directly. The deformed inner radius r_i can be calculated from the incompressibility condition, see (11) in [40], and the isochoric stress components $\sigma_{\theta\theta}^{\mathrm{iso}}(r)$ and $\sigma_{rr}^{\mathrm{iso}}(r)$ are both functions of r because the circumferential and radial stretches depend on the radius [26]. Thus, to numerically determine the internal pressure p_i from the stress through the integration in (47), we need the isochoric stress components at each deformed radius.

For any r contained in $[r_\mathrm{i}, r_\mathrm{o}]$, we can compute the volume enclosed by the surfaces $r = r$, $r = r_\mathrm{i}$, $z = 0$ and $z = l$ as

$$V_r = \pi(r^2 - r_\mathrm{i}^2)l. \tag{48}$$

Then, we assume that r was located at ρ_r in the load-free configuration, see Figures 8(b) and (c), where the volume is

$$V_\rho = \pi(\rho_\mathrm{r}^2 - \rho_\mathrm{i}^2)\xi. \tag{49}$$

Because of the incompressibility ($V_r = V_\rho$), we obtain the load-free radius ρ_r as a continuous function of r, and hence the circumferential stretch is given as a function of r by

$$\lambda_\theta(r) = \frac{r}{\rho_\mathrm{r}(r)} = \frac{r}{\sqrt{\lambda_z(r^2 - r_\mathrm{i}^2) + \rho_\mathrm{i}^2}}. \tag{50}$$

When $r = r_\mathrm{o}$, we recover the stretch at the outer surface $\lambda_{\theta\mathrm{o}}$. With (50) and the measured axial stretch λ_z, we also obtain the radial stretch $\lambda_r(r) = (\lambda_\theta(r)\lambda_z)^{-1}$ as a continuous function of r. Thus, the components of the deformation gradient and the isochoric stress tensor are obtained as functions of r. The internal pressure is then computed using a numerical integration scheme. The five material parameters (μ, k_1, k_2, b, Θ_M) of the fiber dispersion model were determined through a nonlinear least-squares regression (Levenberg–Marquardt algorithm) of the computed pressure against the experimental results; see Figure 9 for the experimental data and model fitting of the internal pressure versus the stretch responses. Due to the lack of structural properties, the mean fiber orientation Θ_M and concentration parameter b are both obtained through the nonlinear least-square regression. The material parameters determined for one representative specimen, an intact common carotid wall from patient II in [39], are summarized in Table 1. The geometry, pressure load and boundary conditions for the finite element model

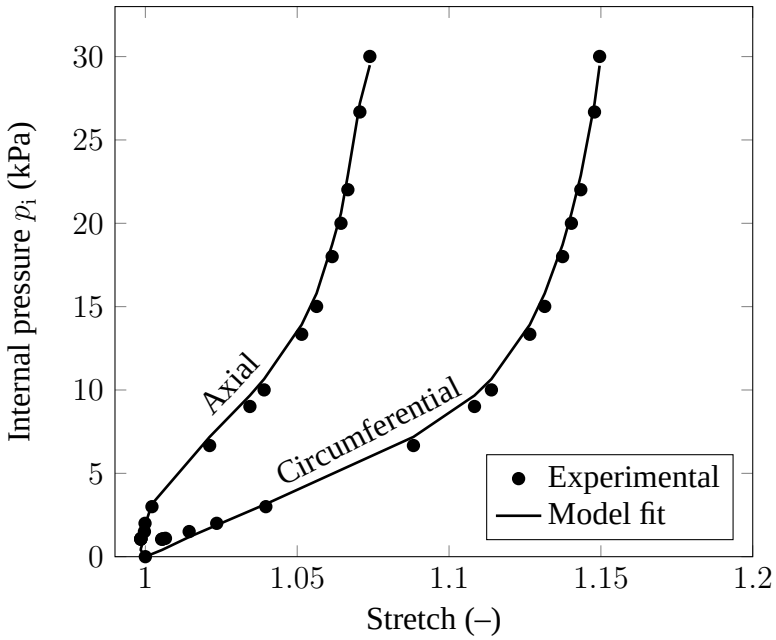

Figure 9: Experimental results according to [39] and model fit of the pressure versus circumferential and axial stretches from a representative human common carotid artery specimen through nonlinear regression.

Table 1: Parameters obtained from experimental data of a human carotid artery [39].

Parameter	μ (kPa)	k_1 (kPa)	k_2 (-)	b (-)	$\Theta_\mathrm{M}\,(^\circ)$
Value	49.31	13.95	13.4	1.2189	40.02

are then obtained from the same arterial segment for which the material parameters were determined.

3.3.2 Finite Element Modeling and Results

To save computational resources, only half the length of the arterial segment was modeled in the finite element simulation. The geometry of the arterial model in the stress-free configuration (see Figure 10(a)) was created based on the same experimental data set from which the material parameters were determined. The length, inner radius and outer radius of the arterial model in the reference configuration are $L = 2.4$ mm, $R_\mathrm{i} = 3.28$ mm and $R_\mathrm{o} = 4.29$ mm, respectively. The opening angle measured from an adjacent thin segment of the same carotid artery is $\alpha = 26.67^\circ$. The geometry of the arterial model was meshed with 576 elements, with four elements through the thickness, see Figure 10(a).

The finite element simulation consists of three steps: closing step, relaxing step and extension–inflation step. In the first step, we gradually close the two cut faces together (see Figure 10(a)) by using the SPIN command in FEAP. All the nodes on the 'symmetry plane' are constrained in the circumferential direction. The axial residual stress was neglected in the simulation. At the end of the closing step the two cut faces coincide, but the 'residual' circumferential stress distribution is not uniform around the circumferential direction. To obtain an evenly distributed residual stress in the circumferential direction, in the second step all the nodes on one cut face are 'glued' together with the corresponding nodes on the other cut face through the ELINK command in FEAP such that there is no relative motion between any pair of coincident nodes. All the constraints on the cut faces imposed by the SPIN command in the first step are removed at this step. To prevent rigid body motion, the four inner nodes of the arterial model on the symmetry plane in both the circumferential and radial directions (see the red nodes in Figure 10(a)) are constrained. At the end of the second step the model is in equilibrium, and the residual stress distribution is uniform in the circumferential direction, see Figure 10(b). Finally, in the third step, the axial constraint on one end of the model is replaced by a time-dependent axial displacement boundary condition which is based on axial stretch measurements obtained from the gage length, see Figure 9, with an axial stretch up to 1.07. A pressure load up to $30\,\text{kPa}$ obtained from the same experiment is applied on the inner surface of the model to inflate the residually stressed artery. The final transmural distribution of the circumferential stress in the arterial model is shown in Figure 10(c).

After the finite element simulation, at each time increment of the third step the outer diameter of the arterial model was computed from the simulation result. The inner pressure versus the circumferential stretch curve from FEAP is compared with the experimental data, see Figure 11. As shown in Figure 11, a good agreement between the FEAP computation and the experimental data has been obtained. Also shown are the FEAP results predicted for the case in which strain energy is computed over the entire half sphere (dashed curve). In this example, we observed a very small difference between these two cases, which can be explained by the surface plots of I_4 and $\rho = \rho_4 + \rho_6$ shown in Figure 12. It can be seen that the region where $I_4 < 1$ contains relatively fewer fibers than the region where $I_4 > 1$. Thus, exclusion of the compressed fibers from the strain-energy function resulted in only a slight change of pressure versus circumferential stretch response. Similarly, we did not observe a significant change of circumferential Cauchy stress due to the exclusion of compressed fibers.

This particular example demonstrates that the exclusion of compressed fibers does not make a significant difference with respect to the all-fiber case. However, for many other examples

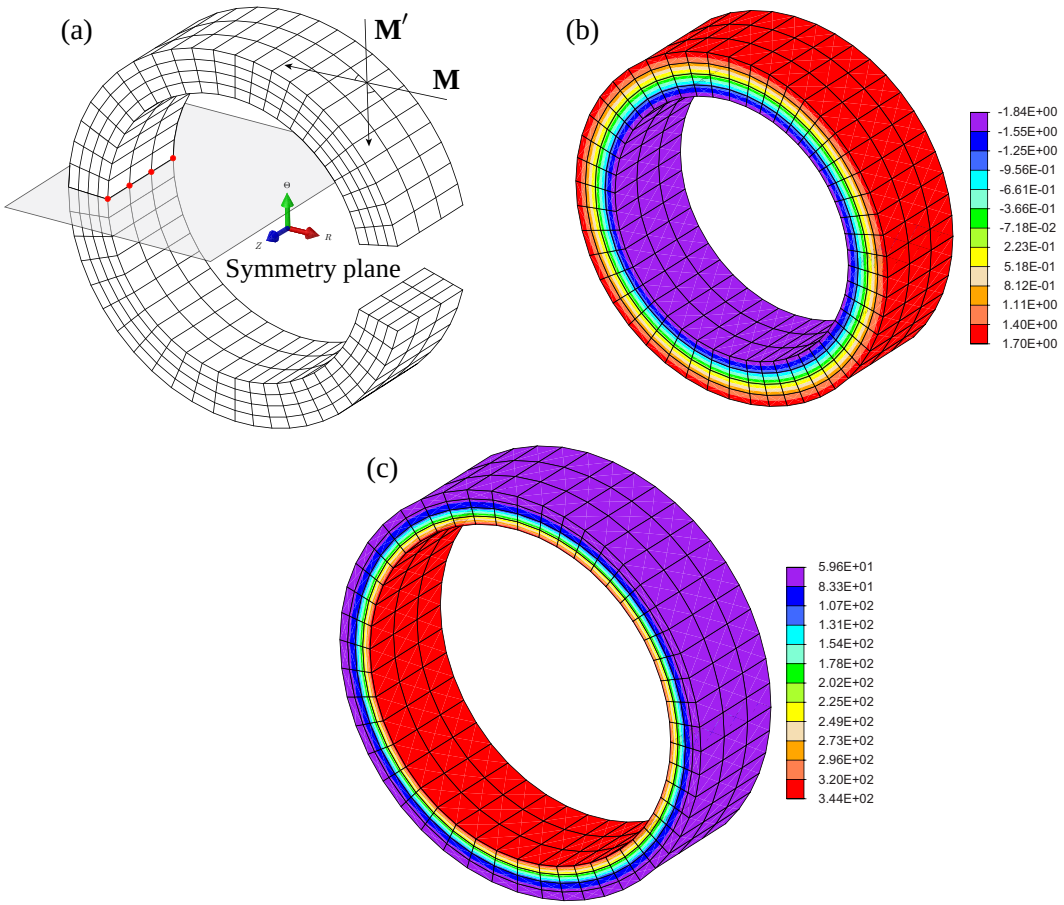

Figure 10: Extension–inflation simulation of a carotid artery with residual stress: (a) finite element model, geometry and symmetry plane (**M** and **M**′ denote the mean fiber directions of the two fiber families); (b) transmural distribution of the residual circumferential stress (kPa) showing compressive stress on the inner region and tensile stress on the outer region; (c) transmural distribution of the circumferential stress (kPa) under an internal pressure of 225 mmHg (30 kPa) and an axial stretch of 1.07 with compressed fibers excluded.

(different boundary-value problems), it makes significant difference, as illustrated in Figure 6 for simple shear. For any considered deformation it depends on what proportion of the fibers are under compression.

4 Concluding Remarks

Our previous work [17, 23] on the constitutive modeling of collagen fiber dispersion in which contributions to the strain-energy function from only those fibers under tension were included was based on a simple fiber reinforcing model. In the present study this work has been extended

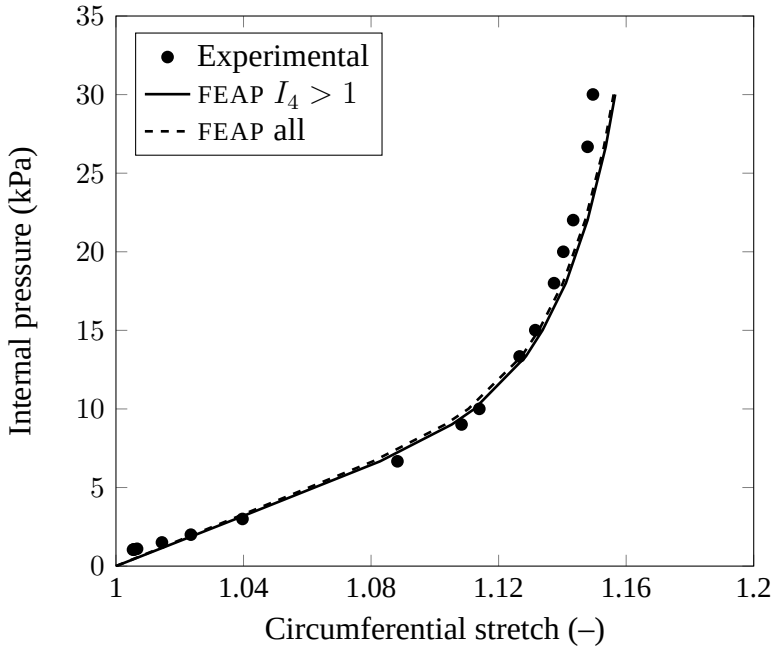

Figure 11: Comparison of the FEAP prediction of pressure versus circumferential stretch with experimental data. The solid curve shows the case with integration over the domain $I_4 > 1$, and the dashed curve shows the case with integration over the entire half sphere including compressed fibers. The dots correspond to experimental data.

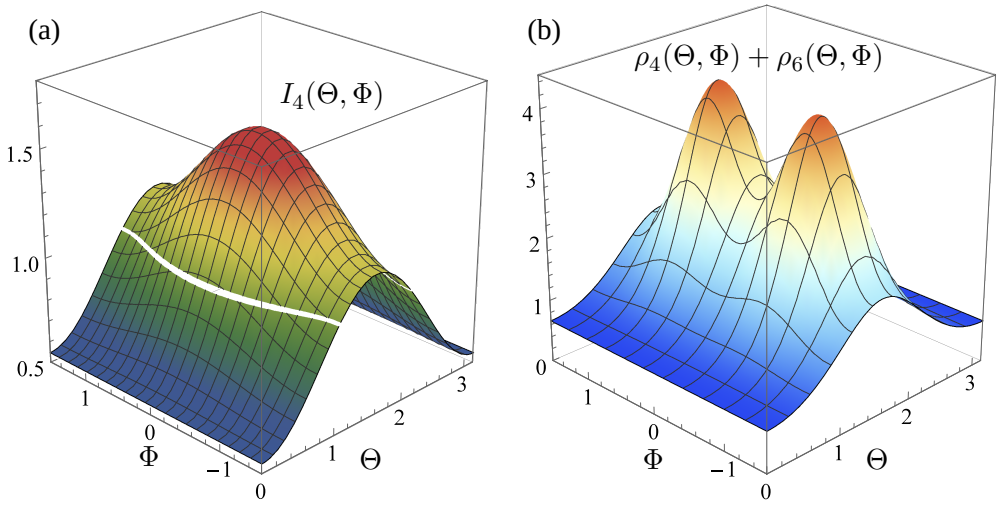

Figure 12: Surface contour plots of (a) $I_4(\Theta, \Phi)$ and (b) $\rho(\Theta, \Phi) = \rho_4(\Theta, \Phi) + \rho_6(\Theta, \Phi)$ for the two fiber families for the extension–inflation test of carotid artery within the half sphere $\mathbb{S}$ defined with respect to the local coordinate system constructed from the eigenvectors of $\mathbf{C}$ ($b = 1.2189$, $p_i = 225$ mmHg). The small gap in (a) represents $I_4 = 1$.

to an exponential form of the strain-energy function for the fiber reinforcement in order to fit experimental data obtained from human tissues. After introducing the mathematical form of the constitutive equation for general 3D fiber dispersions based on the angular integration (AI) approach, we have presented analytical expressions for the Cauchy stress and the Eulerian elasticity tensors in decoupled forms suitable for large scale finite element implementation. Next, we demonstrated the performance of the proposed model with three numerical simulations. It was shown that the exponential form of the strain-energy function is capable of modeling the highly nonlinear behavior of arterial tissue considered here; such a good agreement between model results and experimental data is impossible to achieve with, e.g., a standard fiber-reinforcing model, as used in [23]. The formulation presented here and its computational implementation can be extended straightforwardly to accommodate the recently observed non-symmetric collagen fiber dispersion in arterial walls [16]; this will be the subject of future work. Comparing with the numerical integration rule over the entire unit sphere, the exclusion of compressed fibers within a unit sphere requires more computational time. Thus, parallel computation on a high-performance computer cluster is recommended.

In our last example, we have shown that the considered fiber dispersion model is able to capture the experimentally observed response of a residually stressed carotid artery under extension and inflation. In Figure 10(c) we have observed a high transmural gradient of circumferential stress. This can be explained as follows: (i) a high pressure of 30 kPa was applied to the artery. Such a high pressure could cause a high transmural stress gradient even when the residual stress is considered; (ii) experimental data were obtained from an 80-year old female patient with metastasis and medium grade atherosclerosis in the aorta, which suggests that a larger stress may occur in the intimal layer of a carotid artery if atherosclerosis is present in it too; (iii) the effect of smooth muscle activation has been shown to further homogenize the transmural stress distribution [36], but was neglected in the present study.

In addition, due to the absence of detailed material and structural data for each layer of the carotid artery we modeled the intact arterial wall as a one-layer and thick–walled cylindrical tube. A future study incorporating smooth muscle activation, patient–specific arterial geometry and layer–specific material and structural information, i.e. collagen fiber orientation and distribution, will lead to a more realistic model, the predictions of which will offer important insights.

Acknowledgments

We would like to acknowledge the use of HPC resources provided by the Information Technology Services (ZID) of Graz University of Technology, Austria. We also wish to thank Dr. Gerhard Sommer, Graz University of Technology, for providing the extension–inflation data of a human carotid artery. KL is grateful to the thoughtful discussions with and technical assistance from Professor Robert L. Taylor, University of California, Berkeley, USA, on the implementation of the constitutive model and simulating residual stress in FEAP.

Appendix A: Derivations of Stress and Elasticity Tensors

Derivation of Stress Tensor (14)

Because the boundary of the integration domain Ω in the fiber part of the strain-energy function (12) also depends on the deformation through $\mathbf{C}$, differentiation of the strain energy of the fiber contributions with respect to $\mathbf{C}$ following the Leibniz integral rule for multidimensional integrals reads (without the factor $1/\pi$)

$$\frac{\partial}{\partial\overline{\mathbf{C}}}\iint\limits_{\Omega(\mathbf{C})} F(\overline{\mathbf{C}},\Theta,\Phi)\,\mathrm{d}\Omega = \iint\limits_{\Omega(\mathbf{C})} \frac{\partial}{\partial\overline{\mathbf{C}}}F(\overline{\mathbf{C}},\Theta,\Phi)\,\mathrm{d}\Omega + \int\limits_{\partial\Omega(\mathbf{C})} F(\overline{\mathbf{C}},\Theta,\Phi)\boldsymbol{\mathcal{N}}\otimes\boldsymbol{\mathcal{N}}\,\mathrm{d}s, \qquad (51)$$

where $F(\overline{\mathbf{C}},\Theta,\Phi) = \rho(\Theta,\Phi)\Psi_{\mathrm{n}}(\bar{I}_4(\Theta,\Phi))$ and $\partial\Omega(\mathbf{C})$, with unit outward normal $\boldsymbol{\mathcal{N}}$, denotes the boundary of Ω. Because $I_4 = 1$ on the boundary and for strict incompressibility J approaches 1, we obtain $\lim_{J\to 1}\bar{I}_4 = 1$. Then, $F(\overline{\mathbf{C}},\Theta,\Phi)$ approaches 0 since, from (7), $\Psi_{\mathrm{n}}(1) = 0$. Thus, the second term on the right hand side of (51) vanishes, and does not appear in (14).

Derivation of Elasticity Tensor (20)

Similarly to the result in (51), the second differentiation of the strain-energy function due to fiber contributions with respect to $\mathbf{C}$ reads (without the factor $1/\pi$)

$$\begin{aligned}\frac{\partial}{\partial\overline{\mathbf{C}}}\iint\limits_{\Omega(\mathbf{C})}\frac{\partial}{\partial\overline{\mathbf{C}}}F(\overline{\mathbf{C}},\Theta,\Phi)\,\mathrm{d}\Omega = &\iint\limits_{\Omega(\mathbf{C})}\frac{\partial^2}{\partial\overline{\mathbf{C}}\partial\overline{\mathbf{C}}}F(\overline{\mathbf{C}},\Theta,\Phi)\,\mathrm{d}\Omega \\ &+\int\limits_{\partial\Omega(\mathbf{C})}\frac{\partial}{\partial\overline{\mathbf{C}}}F(\overline{\mathbf{C}},\Theta,\Phi)\otimes\boldsymbol{\mathcal{N}}\otimes\boldsymbol{\mathcal{N}}\,\mathrm{d}s. \qquad (52)\end{aligned}$$

Again, because on the boundary $I_4 = 1$ in the incompressible limit, the second term on the right hand side of (52) vanishes, since, from (7), $\Psi'_{\rm n}(1) = 0$. Thus, the latter term in (52) does not appear in (20).

References

[1] A. J. Schriefl, H. Wolinski, P. Regitnig, S. D. Kohlwein, and G. A. Holzapfel. An automated approach for 3D quantification of fibrillar structures in optically cleared soft biological tissues. *J. R. Soc. Interface*, 10:20120760, 2013.

[2] L. Azinfar, M. Ravanfar, Y. Wang, K. Zhang, D. Duan, and G. Yao. High resolution imaging of the fibrous microstructure in bovine common carotid artery using optical polarization tractography. *J. Biophotonics*, DOI: 10.1002/jbio.201500229, 2016.

[3] S. R. Watson, P. Liu, E. A. Peña, M. A. Sutton, J. F. Eberth, and S. M. Lessner. Comparison of aortic collagen fiber angle distribution in mouse models of atherosclerosis using second-harmonic generation (SHG) microscopy. *Microsc. Microanal.*, 22:55–62, 2016

[4] P. Sáez, A. García, E. Peña, T. C. Gasser, and M. A. Martínez. Microstructural quantification of collagen fiber orientations and its integration in constitutive modeling of the porcine carotid artery. *Acta Biomaterialia*, 33:183–193, 2016.

[5] A. J. Schriefl, G. Zeindlinger, D. M. Pierce, P. Regitnig, and G. A. Holzapfel. Determination of the layer-specific distributed collagen fiber orientations in human thoracic and abdominal aortas and common iliac arteries. *J. R. Soc. Interface*, 9:1275–1286, 2012.

[6] P. B. Canham, H. M. Finlay, J. G. Dixon, D. R. Boughner, and A. Chen. Measurements from light and polarised light microscopy of human coronary arteries fixed at distending pressure. *Cardiovasc. Res.*, 23:973–982, 1989.

[7] H. M. Finlay, L. McCullough, and P. B. Canham. Three-dimensional collagen organization of human brain arteries at different transmural pressures. *J. Vasc. Res.*, 32:301–312, 1995.

[8] H. M. Finlay, P. Whittaker, and P. B. Canham. Collagen organization in the branching region of human brain arteries. *Stroke*, 29:1595–1601, 1998.

[9] W. J. Karlon, J. W. Covell, A. D. McCulloch, J. J. Hunter, and J. H. Omens. Automated measurement of myofiber disarray in transgenic mice with ventricular expression of ras. *Anat. Rec.*, 252:612–625, 1998.

[10] J. W. Covell. Tissue structure and ventricular wall mechanics. *Circulation*, 118:699–701, 2008.

[11] C. Boote, S. Dennis, and K. Meek. Spatial mapping of collagen fibril organisation in primate cornea-an X-ray diffraction investigation. *J. Struct. Biol.*, 146:359–367, 2004.

[12] C. Boote, S. Dennis, Y. Huang, A. J. Quantock, and K. M. Meek. Lamellar orientation in human cornea in relation to mechanical properties. *J. Struct. Biol.*, 149:1–6, 2005.

[13] M. B. Lilledahl, D. M. Pierce, T. Ricken, G. A. Holzapfel, and C. de Lange Davies. Structural analysis of articular cartilage using multiphoton microscopy: input for biomechanical modeling. *IEEE Trans. Med. Imaging*, 30:1635–1648, 2011.

[14] Y. Lanir. Constitutive equations for fibrous connective tissues. *J. Biomech.*, 16:1–12, 1983.

[15] T. C. Gasser, R. W. Ogden, and G. A. Holzapfel. Hyperelastic modelling of arterial layers with distributed collagen fibre orientations. *J. R. Soc. Interface*, 3:15–35, 2006.

[16] G. A. Holzapfel, J. A. Niestrawska, R. W. Ogden, A. J. Reinisch, and A. J. Schriefl. Modelling non-symmetric collagen fibre dispersion in arterial walls. *J. R. Soc. Interface*, 12:20150188, 2015.

[17] G. A. Holzapfel and R. W. Ogden. On the tension–compression switch in soft fibrous solids. *Eur. J. Mech. A/Solids*, 49:561–569, 2015.

[18] G. A. Ateshian, V. Rajan, N. O. Chahine, C. E. Canal, and C. T. Hung. Modeling the matrix of articular cartilage using a continuous fiber angular distribution predicts many observed phenomena. *J. Biomech. Eng.*, 131:61003, 2009.

[19] S. Federico and T. C. Gasser. Nonlinear elasticity of biological tissues with statistical fibre orientation. *J. R. Soc. Interface*, 7:955–966, 2010.

[20] A. V. Melnik, H. Borja Da Rocha, and A. Goriely. On the modeling of fiber dispersion in fiber-reinforced elastic materials. *Int. J. Non-Linear Mech.*, 75:92–106, 2015.

[21] S. Heo and Y. Xu. Constructing fully symmetric cubature formulae for the sphere. *Math. Comput.*, 70:269–279, 2001.

[22] M. Latorre and F. J. Montáns. On the tension-compression switch of the Gasser–Ogden–Holzapfel model: Analysis and a new pre-integrated proposal. *J. Mech. Behav. Biomed. Mater.*, 57:175–189, 2016.

[23] K. Li, R. W. Ogden, and G. A. Holzapfel. Computational method for excluding fibers under compression in modeling soft fibrous solids. *Eur. J. Mech. A/Solids*, 57:178-193, 2016.

[24] Taylor, R.L. *FEAP – A Finite Element Analysis Program, Version 8.4 User Manual*. University of California at Berkeley, Berkeley, California, 2013.

[25] G. Y. Qiu and T. J. Pence. Remarks on the behavior of simple directionally reinforced incompressible nonlinearly elastic solids. *J. Elasticity*, 49:1–30, 1997.

[26] G. A. Holzapfel, T. C. Gasser, and R. W. Ogden. A new constitutive framework for arterial wall mechanics and a comparative study of material models. *J. Elasticity*, 61:1–48, 2000.

[27] P. J. Flory. Thermodynamic relations for highly elastic materials. *Trans. Faraday Soc.*, 57:829–838, 1961.

[28] R. W. Ogden. Nearly isochoric elastic deformations: Application to rubberlike solids. *J. Mech. Phys. Solids*, 26:37–57, 1978.

[29] J. C. Simo. Numerical Analysis and Simulation of Plasticity. In: P. G. Ciarlet and J. L. Lions (Eds), *Handbook of Numerical Analysis*, Vol. VI, Numerical Methods for Solids (Part 3), North-Holland, Elsevier, Amsterdam, 183–499, 1998.

[30] G. A. Holzapfel. *Nonlinear Solid Mechanics. A Continuum Approach for Engineering*. John Wiley & Sons, Chichester, 2000.

[31] G. A. Holzapfel, M. J. Unterberger, and R. W. Ogden. An affine continuum mechanical model for cross-linked F-actin networks with compliant linker proteins. *J. Mech. Behav. Biomed. Mater.*, 38:78–90, 2014.

[32] J. C. Simo and R. L. Taylor. Quasi-incompressible finite elasticity in principal stretches. Continuum basis and numerical algorithms. *Comput. Meth. Appl. Mech. Eng.*, 85:273–310, 1991.

[33] J. C. Simo, R. L. Taylor, and K. S. Pister. Variational and projection methods for the volume constraint in finite deformation elasto-plasticity. *Comput. Meth. Appl. Mech. Eng.*, 51:177–208, 1985.

[34] MATLAB R2016a, The MathWorks Inc., Natick, MA, USA, 2016.

[35] Wolfram Research, Inc., Mathematica, Version 10.5, Champaign, IL, USA, 2016.

[36] J. D. Humphrey and S. Na. Elastodynamics and arterial wall stress. *Annals of Biomedical Engineering.*, 30:509–523, 2002.

[37] G. A. Holzapfel and R. W. Ogden. Modelling the layer-specific three-dimensional residual stresses in arteries, with an application to the human aorta. *J. R. Soc. Interface*, 7:787–799, 2010.

[38] C. J. Chuong and Y. C. Fung. On residual stresses in arteries. *ASME J. Biomech. Eng.*, 108:186–192, 1986.

[39] G. Sommer, P. Regitnig, L. Költringer, and G. A. Holzapfel. Biaxial mechanical properties of intact and layer-dissected human carotid arteries at physiological and supraphysiological loadings. *Am. J. Physiol. Heart Circ. Physiol.*, 298:H898–912, 2010.

[40] G. Sommer and G. A. Holzapfel. 3D constitutive modeling of the biaxial mechanical response of intact and layer-dissected human carotid arteries. *J. Mech. Behav. Biomed. Mater.*, 5:116–128, 2012.